Weakening of nonlinear ENSO under global warming

Tsubasa Kohyama[1], Dennis L. Hartmann[1], and David S. Battisti[1]

Key points:

- Model experiments show that the nonlinearity of ENSO can weaken the ENSO amplitude under global warming
- Increased upper ocean thermal stratification inhibits thermocline depth variations and nonlinear temperature responses
- Observations exhibit stronger thermal stratification than models, suggesting that nonlinear ENSO weakening may occur in the real world

Corresponding author: T. Kohyama, Department of Atmospheric Sciences, University of Washington, 408 Atmospheric Sciences-Geophysics (ATG) Building, Box 351640, Seattle WA 98195-1640, USA. (kohyama@uw.edu)

[1]Department of Atmospheric Sciences,
University of Washington, Seattle,
Washington, USA.

Abstract. The ENSO amplitude response to global warming is examined in two global climate models with realistic nonlinearity of the El Niño Southern Oscillation (ENSO). GFDL-ESM2M and MIROC5 are the two models that exhibit realistic ENSO nonlinearity. With quadrupled atmospheric carbon dioxide, the ENSO amplitude of GFDL-ESM2M decreases by about 40%, whereas that of MIROC5 remains almost constant. Because GFDL-ESM2M exhibits stronger climatological thermal stratification than MIROC5, greenhouse gas forcing increases the upper ocean stability and causes the thermocline to be less sensitive to wind perturbations. The stiffer thermocline inhibits the nonlinear variations of subsurface temperature so that the ENSO amplitude substantially weakens. Idealized nonlinear recharge oscillator model experiments further support climatological thermal stratification as a determinant of the warming response. Observations exhibit stronger thermal stratification than both models, so the real world may terminate strong, nonlinear El Niños sooner than model-based projections.

Index terms: 1626 Global climate models, 3339 Ocean/atmosphere interactions, 3373 Tropical dynamics, 4522 ENSO

Keywords: Global Warming, ENSO amplitude, ENSO nonlinearity

1. Introduction

The tropical Pacific Ocean has attracted attention in physical climatology, because its variability influences the climate all over the Earth [e.g., *Horel and Wallace*, 1981; *Rasmusson et al.*, 1983]. The El Niño Southern Oscillation (ENSO) is a dominant mode of variability that explains the largest variance of tropical Pacific sea surface temperature (SST), so the response of ENSO to global warming is of great interest for the future climate [e.g., *Collins et al.*, 2010; *Christensen et al.*, 2013; *Kim et al.*, 2014]. State-of-the-art global climate models (GCM), however, have had difficulty reproducing the features of the observed ENSO, including its amplitude, irregular frequency, non-Gaussianity, and their impacts on the extratropics [e.g., *Collins et al.*, 2010; *Bellenger et al.*, 2014; *Zhang and Sun*, 2014]. Weaknesses in the simulation of ENSO render large uncertainty in the warming response of the entire climate system [e.g., *Yokoi and Takayabu*, 2009; *Murakami et al.*, 2012; *Christensen et al.*, 2013; *Kohyama and Hartmann*, 2016].

Despite the difficulty of simulating ENSO, it has been common to choose a subset of GCMs that reproduce a particular observed feature well, and to assume that this subset makes more reliable future projections than the multi-model mean [e.g., *Risbey et al.*, 2014]. Based on this assumption, we project the future ENSO amplitude responses using two GCMs that realistically reproduce the observed ENSO nonlinearity, because of which warm anomalies tend to be larger than cold anomalies (El Niños tend to be stronger than La Niñas). Figure 1a shows the relationship between the ENSO skewness (a measure of the ENSO nonlinearity) and the zonal SST gradient change simulated by GCMs under global warming. This figure shows that the Geophysical Fluid Dynamics Laboratory

Earth System Model Version 2M (GFDL-ESM2M) [*Dunne et al.*, 2012, 2013] and the Model for Interdisciplinary Research on Climate version 5 (MIROC5) [*Watanabe et al.*, 2010] are the two models that reproduce the observed ENSO skewness better than most of the other models that participated in the Coupled Model Intercomparison Project Phase 5 (CMIP5) [*Taylor et al.*, 2012]. We analyze these two GCMs.

Figure 1b shows the time series of SST anomalies averaged over the Niño3 region (5°S-5°N, 150°W-90°W), a common index of ENSO. The left column shows the Niño3 SST for the historical climate of the two GCMs. Though GFDL-ESM2M exhibits an excessively large ENSO variance, both models exhibit realistic ENSO nonlinearity as suggested in Fig. 1a quantitatively. The right column shows the same time series but for a warmer climate. Interestingly, compared to the historical climate, the ENSO amplitude of GFDL-ESM2M is reduced by about 40% in its standard deviation, whereas that of MIROC5 remains almost constant in a warmed climate. Our motivations are to understand this difference in the amplitude responses and to make a physically reasonable projection of the future ENSO change.

Recent studies that link the projected change in the mean-state tropical Pacific SST to the ENSO nonlinearity further motivates us to proceed in this venue. We hereafter call a mean-state response “El Niño-like” when the eastern equatorial Pacific warms faster than the west, and the opposite response “La Niña-like” [*Collins et al.*, 2005; *Held et al.*, 2010; *An et al.*, 2012]. Despite the El Niño-like warming response projected by the majority of the CMIP5 models [e.g., *Ying et al.*, 2016; *Zheng et al.*, 2016], *Kohyama et al.* [2017] and *Kohyama and Hartmann* [2017] showed that, given the realistic ENSO nonlinearity, a La Niña-like response also remains physically consistent. In GFDL-ESM2M, the ENSO nonlinearity is minimized under global warming, and the extreme El Niños dissipate, but La Niñas remain almost unchanged. This asymmetric weakening response can rectify the mean-state SST to become La Niña-like, and this mechanism is referred to as the nonlinear ENSO warming suppression (NEWS). *Kohyama and Hartmann* [2017] concluded that a necessary condition to simulate NEWS is realistic ENSO skewness, and the lack thereof is why most CMIP5 models exhibit El Niño-like responses.

Realistic ENSO skewness, however, is not a sufficient condition to simulate NEWS. Figures 1a and 1c show that, though both GFDL-ESM2M and MIROC5 exhibit realistic ENSO skewness, MIROC5 exhibits a strong El Niño-like response unlike GFDL-ESM2M. This difference motivates us to understand why the ENSO nonlinearity is not the only requirement for a La Niña-like response.

This article is organized as follows. Data and methods are described in the next section. In section 3, we show that the response of subsurface temperature to the thermocline depth anomalies is the source of the ENSO nonlinearity in these models. Then, we propose a nonlinear mechanism for how the climatological upper ocean thermal stratification determines the ENSO amplitude response to warming. We also compare the observed thermal stratification with the modeled ones. Conclusions are presented in section 4.

2. Data and Methods

2.1. Data

The monthly surface temperature, oceanic potential temperature, and wind stress output of GFDL-ESM2M [*Dunne et al.*, 2012, 2013] are from the GFDL Data Portal (http://nomads.gfdl.noaa.gov:8080/DataPortal/cmip5.jsp), and those of MIROC5 [*Watanabe et al.*, 2010] are from the Program for Climate Model Diagnosis and Intercomparison (https://pcmdi.llnl.gov/projects/cmip5/). We analyze the first ensemble member of the historical (Years 1966-2005) and abrupt4xCO_2 runs (Years 101-150 after the abrupt change are used). In the Abrupt4xCO_2 runs, Year 101 starts when 100 years have passed after the abrupt quadrupling of carbon dioxide, and the qualitative argument regarding the ENSO amplitude is not sensitive to this choice of the 50-yr time span [see also *Kohyama and Hartmann*, 2017]. At each depth, the oceanic variables are regridded using linear interpolation onto a 2.5° longitude by 2° latitude grid. To produce Fig. 1, the first ensemble member of the representative concentration pathway (RCP) 8.5 (Year 2006-2100) runs are used. Detailed descriptions of the CMIP5 project are presented by *Taylor et al.* [2012].

The reanalysis monthly oceanic potential temperature is from the National Centers for Environmental Prediction (NCEP) Global Ocean Data Assimilation System (GODAS) [*Behringer and Xue*, 2004] at http://www.esrl.noaa.gov/psd/data/gridded/data.godas.html. The horizontal resolution is 1° longitude by 1/3° latitude, and the vertical resolution is 10 m for uppermost 230 m and becomes coarser toward the deeper levels. The zonal wind field at the 10 m level and the SST are from the European Center for Medium range Weather Forecasting (ECMWF) ERA-Interim reanalysis data [*Dee et al.*, 2011] at http://apps.ecmwf.int/datasets/data/interim-full-moda/levtype=sfc/. The resolution is 1° in both longitude and latitude. The time span used in this study is from 1980 through 2016 for all the reanalysis data.

2.2. Methods

2.2.1. Decomposing the sources of the ENSO nonlinearity

Following *An and Kim* [2017], we decompose the source of the ENSO nonlinearity into three components: (i) “SST modulates winds”, (ii) “winds excite oceanic waves”, and (iii) “oceanic waves that have propagated to the east modulate subsurface temperature”. To measure the relative impact of these 3 sources of nonlinearity, we draw scatter plots between two area-averaged anomalies in the manner of: (i) SST (170°W-120°W, 5°S-5°N) and zonal wind stress (120°E-80°W, 5°S-5°N); (ii) zonal wind stress (120°E-80°W, 5°S-5°N) and thermocline depth (120°E-80°W, 5°S-5°N); (iii) eastern thermocline depth (170°W-120°W, 5°S-5°N) and subsurface temperature at a depth of 45 m (170°W-120°W, 5°S-5°N). These anomalies are deviations from monthly climatology calculated as the average over the full time span for each calendar month. The thermocline depth is defined as the level of maximum vertical temperature gradient. For observations, 10 m wind is used as a proxy of wind stress.

To draw each scatter plot, we first calculate the lead-lag relationship between the two variables and choose the lags with maximum correlations. The chosen lags are within a half-year difference from the results shown in *An and Kim* [2017], which are (i) zero-lag, (ii) wind stress leads the thermocline depth by 12-months, and (iii) the thermocline depth leads subsurface temperature by 3 months. For further physical explanation, readers are referred to *An and Kim* [2017].

The best-fit lines are drawn based on the standardized data. Linear regression and principle component analysis yield almost identical linear fits. In Fig. 2, following *An* *and Kim* [2017], the asymmetry index is defined as

$$\mathrm{Asym} = \frac{S_p - S_n}{S_p + S_n} \tag{1}$$

where S_p (S_n) is the slope of the red (blue) best-fit lines calculated using the data only with the positive (negative) values in the horizontal axis. In Fig. 3, after drawing the best-fit lines, the original standard deviations are multiplied back so that the data have physical units.

2.2.2. Idealized model

We use a modified version of the nonlinear recharge oscillator ENSO model introduced by *Jin* [1998] and *Timmermann et al.* [2003]. This model is a simplified, two-box approximation of the Cane-Zebiak model [*Zebiak and Cane*, 1987]. Detailed descriptions of the model and our modifications are given in *Kohyama and Hartmann* [2017].

3. Results

3.1. Source of the ENSO nonlinearity

Figure 2a shows the observed three potential sources of ENSO nonlinearity. Among the three, the asymmetry index is largest for (iii), so the observational ENSO nonlinearity mainly originates from the subsurface temperature response to oceanic waves. This result may appear inconsistent with *An and Kim* [2017] who showed that (ii) is the source of the nonlinearity. This inconsistency, however, may originate from their method to calculate the thermocline depth. *An and Kim* [2017] used the 17°C isotherm as a proxy of the thermocline, and we have confirmed that a similar conclusion to their study is derived by doing so. Nevertheless, by definition, the depth of the maximum vertical temperature gradient is a more appropriate measure of the thermocline depth. Though the proxy of the

17°C isotherm works well when linearity is assumed, it is not ideal to use it for investigating nonlinearity, because the difference between the location of the 17°C isotherm and the maximum temperature gradient may yield spurious nonlinearity or cancel true nonlinear signals.

Figure 2b shows the same scatter plots but for the historical runs of GFDL-ESM2M and MIROC5. These two GCMs reproduce the observed relationships of (i)-(iii) well, suggesting that the source of the nonlinearity in the model is (iii). The responses to increasing CO2 are different between the two GCMs, however. Figure 2c shows the same plots but for the warmer climate, where the (iii) component becomes virtually linear in GFDL-ESM2M but not in MIROC5. The asymmetry index of (iii) in GFDL-ESM2M changes from 0.97 to 0.22 with warming, whereas in MIROC5 only from 0.90 to 0.81. Though the mechanism for the ENSO nonlinearity for the historical climate is similar between the two models, the warming response of nonlinearity is different.

3.2. Mechanism for the different ENSO warming responses

Kohyama and Hartmann [2017] concluded that the climatological temperature difference between the atmosphere near the surface and the ocean below the thermocline serves as a determinant of the nonlinear response to warming. Therefore, we first compare the climatological upper ocean temperature between the two models.

Figure 3a shows the equatorial climatological temperature difference between the two models. For the historical climate, temperature below the thermocline is cooler in GFDL-ESM2M than in MIROC5, whereas temperature above the thermocline is warmer (Fig. 3a, top). That is, the equatorial ocean interior is more thermally stratified and stable in

GFDL-ESM2M than in MIROC5. This difference in the stability becomes more evident in the warmer experiment (Fig. 3a, bottom). This intensification of the stability difference under global warming may be due to a positive feedback as follows. If the ocean is more stable, the warmer water in the upper ocean is less likely to be vertically mixed with the colder water in the deeper ocean. The suppressed vertical heat exchange further stabilizes the system.

If the ocean becomes more stable, the equatorial thermocline becomes less sensitive to winds due to the following mechanism. Figure 3c shows a schematic of the equatorial thermocline presented as a 1.5-layer model. Hydrostatic balance and no motion in the lower layer are assumed, because in principle, no energy enters the lower layer at sufficiently high frequencies. Hence, the pressure gradient at a reference level in the lower layer is zero:

$$\rho_1 h_1 + \rho_2 h_2 = \rho_1 h_3 + \rho_2 h_4 \tag{2}$$

or

$$\rho_1 \frac{h_1 - h_3}{L} = \rho_2 \frac{h_4 - h_2}{L} \tag{3}$$

where L denotes the width of the basin in the longitudinal direction, ρ_1 (ρ_2) denotes the upper (lower) layer density, and h_i denotes the layer depth. For h_i, the index i denotes the upper (lower) layer by $i = 1, 3$ ($i = 2, 4$), and the western (eastern) edge of the basin by $i = 1, 2$ ($i = 3, 4$) as described in Fig. 3c. Using the definition of the slopes, $-\alpha \equiv \{(h_3 + h_4) - (h_1 + h_2)\}/L$ and $\beta \equiv (h_4 - h_2)/L$ where $\alpha > 0$, $\beta > 0$, we get

$$\rho_1(\alpha + \beta) = \rho_2 \beta \tag{4}$$

or

$$\beta = \frac{\alpha}{\rho_2/\rho_1 - 1} \tag{5}$$

Differentiating both sides, and assuming that the easterly wind stress anomalies ($-d\tau$) is proportional to the sea level tilt anomalies ($d\alpha \propto -d\tau$) [*Li and Clarke*, 1994], we get

$$d\beta \propto -\frac{d\tau}{\rho_2/\rho_1 - 1} \tag{6}$$

This equation 6 means that the sensitivity of the thermocline tilt anomalies to wind stress, or $1/(\rho_2/\rho_1 - 1)$, depends upon the ratio of the densities between the two layers. Therefore, if the ocean becomes more stable as the climate warms, the denominator $\rho_2/\rho_1 - 1$ becomes larger and the equatorial thermocline depth becomes less sensitive to winds, as schematically shown in Fig. 4d. Using the reduced gravity $g' = g(\rho_2/\rho_1 - 1)$, the equation (6) could be also written as

$$d\beta \propto -\frac{d\tau}{g'} \tag{7}$$

where the constant g is omitted. Equations 6 and 7 both indicate that the thermocline slope is less sensitive to wind stress for a more stable ocean.

Based on this mechanism, the sensitivity of thermocline to winds shown in Fig. 3b is consistent with the thermal stratification shown in Fig. 3a. For the historical climate, GFDL-ESM2M has a more stable ocean and exhibits a smaller sensitivity of the thermocline to winds than MIROC5 by about 30 %. We could call the thermocline in GFDL-ESM2M "stiffer" than in MIROC5. For the warmer climate, the difference in thermocline sensitivity between the two models becomes larger, because the upper ocean in GFDL-ESM2M warms faster and the stability is increased more.

Because the thermocline varies less in GFDL-ESM2M, equatorial waves with large amplitudes are hard to excite, and the resultant modulations of the eastern thermocline are also minimized. Figure 3e robustly shows that, in the warmer experiment in GFDL-ESM2M, the subsurface temperature does not "swing" enough to support a large ENSO amplitude due to the lack of perturbations by waves. This small amplitude appears to be why the ENSO in GFDL-ESM2M becomes almost linear for the warmer climate. In MIROC5, however, the variations of the eastern thermocline are kept large enough to sustain the nonlinear response of subsurface temperature. Due to the weak historical thermal stratification, the thermal stratification in MIROC5 does not become stronger as rapidly as in GFDL-ESM2M. Due to the small stability, the thermocline responds strongly to winds. This more "reactive" thermocline allows larger anomalies to enter the eastern thermocline, which supports strong, nonlinear subsurface temperature variations.

3.3. Idealized model experiments

To verify the mechanism by numerical simulations, we have performed two idealized model experiments with different stability. In the "More Stable" experiment (Fig. 4a, top), the temperature difference between the atmosphere near the surface and the ocean below the thermocline ($T_a - T_o$) is initially set to be 13.5 °C, and the $T_a - T_o$ is increased with the rate of 0.7 °C / century, expressing that the atmosphere warms faster than the ocean due to the different heat capacity. In the "Less Stable" experiment (Fig. 4a, bottom), $T_a - T_o$ is initially set to be 12.5 °C, and the $T_a - T_o$ is increased with the rate of 0.4 °C / century. The $T_a - T_o$ is increased more rapidly in the "More Stable" experiment to incorporate the effect of the suppressed vertical heat exchange.

Figure 4a shows the SST time series in the two experiments. In the "More Stable" experiment, which is designed to imitate GFDL-ESM2M, strong El Niños are terminated at the threshold of $T_a - T_o \sim 14.2°\mathrm{C}$. This termination is because the "stiff" thermocline cannot recharge the heat in the equatorial upper ocean to yield a strong El Niño [*Kohyama and Hartmann*, 2017]. By contrast, in the "Less Stable" experiment, which is designed to imitate MIROC5, strong El Niños are not terminated because $T_a - T_o$ does not reach the threshold of $\sim 14.2°\mathrm{C}$ even after the two-century run. Rather, because of the warming western Pacific, which serves as the upper bound of the ENSO intensity [*An and Jin*, 2004], the ENSO amplitude strengthens by about 10% during the two centuries. This difference in the existence of the nonlinearity termination between the two experiments is consistent with the mechanism explained in the previous subsection.

3.4. Comparison with observations

We also compare the two models with the observations to project the future ENSO change. Figure 4b shows the same temperature plot as in Fig. 3a but for observations relative to the two models. The observed equatorial upper ocean is more stable than the GFDL-ESM2M, which is more stable than MIROC5. This observed strong stability is more favorable for $T_a - T_o$ to reach the threshold that terminates strong El Niño events than in the two models. Though this conclusion is derived only from the two GCMs and idealized model experiments, it makes physical sense to project that, based on the observations and the available models with realistic nonlinearity, ENSO may weaken nonlinearly sooner than the model-based projections.

4. Conclusions

4.1. The ENSO nonlinearity matters to the ENSO and mean-state responses to global warming

Under global warming, the ENSO amplitude in GFDL-ESM2M weakens, but that in MIROC5 remains almost constant (Fig. 1b). Decomposing the potential source of the ENSO nonlinearity into three components, we have demonstrated that the difference in the ENSO amplitude responses between the two models is associated with the nonlinear subsurface temperature response to oceanic waves, rather than the wind response to SST or the oceanic wave response to winds (Figs. 2 and 3e).

Many GCMs show strengthening of ENSO in response to warming [*Collins et al.*, 2010], but they do not reproduce the ENSO nonlinearity as realistically as GFDL-ESM2M and MIROC5 (Fig. 1a). Our preliminary analysis suggests that many CMIP5 models do not reproduce the nonlinear subsurface temperature response to waves. Without the possibility of the nonlinear regime shift, one might project that the ENSO amplitude will strengthen. We should, however, pay more attention to the GCMs that reproduce the realistic ENSO nonlinearity, because ENSO in the real world is nonlinear.

Based on the NEWS mechanism proposed by *Kohyama and Hartmann* [2017], the nonlinear ENSO response to global warming can rectify the mean-state SST. Therefore, the difference of the nonlinear ENSO response between GFDL-ESM2M and MIROC5 could have an important implication for whether the response will be El Niño-like or La Niña-like (Fig. 1). Considering the scientific and societal impacts, the ENSO nonlinearity is a key characteristic and should not be considered to be a minor, higher-order correction of the linear ENSO.

4.2. An urgent task is to improve the reproducibility of the thermal stratification in GCMs because it determines the nonlinear ENSO response

With strong climatological thermal stratification in the upper ocean, ENSO may weaken nonlinearly in response to warming. The mechanism is explained as follows. If the thermal stratification becomes stronger, weaker thermocline variations can keep the ocean in hydrostatic balance (Figs. 3c, d and Equation 6). The resultant "stiffer" thermocline depth is less sensitive to winds (Fig. 3b), which minimizes the nonlinear response of the eastern subsurface temperature. Importantly, despite the small difference in thermocline sensitivity, the nonlinearity produces a huge difference in the amplitude of the subsurface temperature (Fig. 3e).

The idealized model confirms that the climatological temperature difference between the atmosphere near the surface and the ocean below the thermocline ($T_a - T_o$) is an important parameter (Fig. 4a). Here, $T_a - T_o$ could be regarded as the first order approximation of the climatological thermal stratification. Once $T_a - T_o$ reaches a certain threshold value, strong El Niños become terminated [see also *Kohyama and Hartmann*, 2017]. This sudden loss of strong El Niños is consistent with the two GCMs. In GFDL-ESM2M, because the thermal stratification is strong, ENSO becomes almost linear. By contrast, ENSO keeps its amplitude in MIROC5, because the weak thermal stratification is unfavorable to reach the threshold for the ENSO to weaken. It might be interesting to warm MIROC5 more and check whether the ENSO in MIROC5 can be weakened.

4.3. Observational thermal stratification suggests that the ENSO amplitude might weaken nonlinearly, and the regime shift might happen sooner than the GCM-based projections

GFDL-ESM2M and MIROC5 suggests that, if $T_a - T_o$ is large for the historical climate, $T_a - T_o$ will increase rapidly under a warming climate (Fig. 3a). This intensification of $T_a - T_o$ makes physical sense, because the suppressed vertical mixing will inhibit the vertical heat exchange. As shown in Fig. 4b, the observed $T_a - T_o$ is larger than the modeled ones for the historical climate. Therefore, the observed strong $T_a - T_o$ may support a rapid increase of $T_a - T_o$ that terminates strong El Niños. GFDL-ESM2M exhibits the termination of strong El Niños in Year 2070 for the RCP8.5 scenario [*Kohyama and Hartmann*, 2017], so the observed strong thermal stratification leads us to speculate that the regime shift might happen in a couple of decades.

Acknowledgments. This study is based on data from the GFDL Data Portal (`http://nomads.gfdl.noaa.gov:8080/DataPortal/cmip5.jsp`), the Program for Climate Model Diagnosis and Intercomparison website (`https://pcmdi.llnl.gov/projects/cmip5/`), and the GODAS dataset (`http://www.esrl.noaa.gov/psd/data/gridded/data.godas.html`). This work was supported by the National Science Foundation (NSF) under grant AGS-1549579 and Takenaka Scholarship Foundation. The third author was funded by the Tamaki foundation. We would like to thank Michiya Hayashi for his useful advice.

References

An, S.-I., and F.-F. Jin (2004), Nonlinearity and asymmetry of ENSO, *J. Climate*, *17*(12), 2399–2412.

An, S.-I., and J.-W. Kim (2017), Role of nonlinear ocean dynamic response to wind on the asymmetrical transition of El Niño and La Niña, *Geophys. Res. Lett.*, *44*(1), 393–400.

An, S.-I., J.-W. Kim, S.-H. Im, B.-M. Kim, and J.-H. Park (2012), Recent and future sea surface temperature trends in tropical Pacific warm pool and cold tongue regions, *Climate Dyn.*, *39*(6), 1373–1383.

Behringer, D., and Y. Xue (2004), Evaluation of the global ocean data assimilation system at NCEP: The Pacific Ocean, in *Proc. Eighth Symp. on Integrated Observing and Assimilation Systems for Atmosphere, Oceans, and Land Surface.*

Bellenger, H., É. Guilyardi, J. Leloup, M. Lengaigne, and J. Vialard (2014), ENSO representation in climate models: from CMIP3 to CMIP5, *Climate Dyn.*, *42*(7-8), 1999–2018.

Christensen, J., K. Krishna Kumar, E. Aldrian, S.-I. An, I. Cavalcanti, M. de Castro, W. Dong, P. Goswami, A. Hall, J. Kanyanga, A. Kitoh, J. Kossin, N.-C. Lau, J. Renwick, D. Stephenson, S.-P. Xie, and T. Zhou (2013), *Climate Phenomena and their Relevance for Future Regional Climate Change*, book section 14, pp. 1217–1308, Cambridge University Press, Cambridge, United Kingdom and New York, NY, USA, doi: 10.1017/CBO9781107415324.028.

Collins, M., S.-I. An, W. Cai, A. Ganachaud, E. Guilyardi, F.-F. Jin, M. Jochum, M. Lengaigne, S. Power, A. Timmermann, et al. (2010), The impact of global warming on the tropical Pacific Ocean and El Niño, *Nature Geosci.*, *3*(6), 391–397.

Collins, M., et al. (2005), El Niño-or La Niña-like climate change?, *Climate Dyn.*, *24*(1), 89–104.

Dee, D. P., S. M. Uppala, A. J. Simmons, P. Berrisford, P. Poli, S. Kobayashi, U. Andrae, M. Balmaseda, G. Balsamo, P. Bauer, P. Bechtold, A. C. M. Beljaars, L. van de Berg, J. Bidlot, N. Bormann, C. Delsol, R. Dragani, M. Fuentes, A. J. Geer, L. Haimberger, S. B. Healy, H. Hersbach, E. V. Hólm, L. Isaksen, P. Kållberg, M. Köhler, M. Matricardi, A. P. McNally, B. M. Monge-Sanz, J.-J. Morcrette, B.-K. Park, C. Peubey, P. de Rosnay, C. Tavolato, J.-N. Thépaut, and F. Vitart (2011), The ERA-interim reanalysis: configuration and performance of the data assimilation system, *Quart. J. Roy. Meteor. Soc.*, *137*, 553,597, doi:10.1002/qj.828.

Dunne, J. P., J. G. John, A. J. Adcroft, S. M. Griffies, R. W. Hallberg, E. Shevliakova, R. J. Stouffer, W. Cooke, K. A. Dunne, M. J. Harrison, et al. (2012), GFDL's ESM2 global coupled climate-carbon Earth System Models. Part I: Physical formulation and baseline simulation characteristics, *J. Climate*, *25*(19), 6646–6665.

Dunne, J. P., J. G. John, E. Shevliakova, R. J. Stouffer, J. P. Krasting, S. L. Malyshev, P. Milly, L. T. Sentman, A. J. Adcroft, W. Cooke, et al. (2013), GFDL 's ESM2 global coupled climate–Carbon Earth System Models. Part II: Carbon system formulation and baseline simulation characteristics, *J. Climate*, *26*(7), 2247–2267.

Held, I. M., M. Winton, K. Takahashi, T. Delworth, F. Zeng, and G. K. Vallis (2010), Probing the fast and slow components of global warming by returning abruptly to preindustrial forcing, *J. Climate*, *23*(9), 2418–2427.

Horel, J. D., and J. M. Wallace (1981), Planetary-scale atmospheric phenomena associated with the southern oscillation, *Mon. Wea. Rev.*, *109*(4), 813–829.

Jin, F.-F. (1998), A simple model for the pacific cold tongue and ENSO, *J. Atmos. Sci.*, *55*(14), 2458–2469.

Kim, S. T., W. Cai, F.-F. Jin, A. Santoso, L. Wu, E. Guilyardi, and S.-I. An (2014), Response of El Niño sea surface temperature variability to greenhouse warming, *Nature Climate Change*, *4*(9), 786–790.

Kohyama, T., and D. L. Hartmann (2016), Antarctic sea ice response to weather and climate modes of variability, *J. Climate*, *29*(2), 721–741.

Kohyama, T., and D. L. Hartmann (2017), Nonlinear ENSO warming suppression (NEWS), *J. Climate*, *30*(11), 4227–4251.

Kohyama, T., D. L. Hartmann, and D. S. Battisti (2017), La niña–like mean-state response to global warming and potential oceanic roles, *J. Climate*, *30*(11), 4207–4225.

Li, B., and A. J. Clarke (1994), An examination of some enso mechanisms using interannual sea level at the eastern and western equatorial boundaries and the zonally averaged equatorial wind, *J. Phys. Oceanogr.*, *24*(3), 681–690.

Murakami, H., R. Mizuta, and E. Shindo (2012), Future changes in tropical cyclone activity projected by multi-physics and multi-sst ensemble experiments using the 60-km-mesh mri-agcm, *Climate Dyn.*, *39*(9-10), 2569–2584.

Rasmusson, E. M., J. M. Wallace, et al. (1983), Meteorological aspects of the el nino/southern oscillation, *Science*, *222*(4629), 1195–1202.

Risbey, J. S., S. Lewandowsky, C. Langlais, D. P. Monselesan, T. J. O 'Kane, and N. Oreskes (2014), Well-estimated global surface warming in climate projections selected for enso phase, *Nature Climate Change*, *4*(9), 835–840.

Taylor, K. E., R. J. Stouffer, and G. A. Meehl (2012), An overview of CMIP5 and the experiment design, *Bull. Amer. Meteor. Soc.*, *93*(4), 485–498.

Timmermann, A., F.-F. Jin, and J. Abshagen (2003), A nonlinear theory for El Niño bursting, *J. Atmos. Sci.*, *60*(1), 152–165.

Watanabe, M., T. Suzuki, R. O 'ishi, Y. Komuro, S. Watanabe, S. Emori, T. Takemura, M. Chikira, T. Ogura, M. Sekiguchi, et al. (2010), Improved climate simulation by MIROC5: mean states, variability, and climate sensitivity, *J. Climate*, *23*(23), 6312–6335.

Ying, J., P. Huang, and R. Huang (2016), Evaluating the formation mechanisms of the equatorial Pacific SST warming pattern in CMIP5 models, *Adv. Atmos. Sci*, *33*(4), 433–441.

Yokoi, S., and Y. N. Takayabu (2009), Multi-model projection of global warming impact on tropical cyclone genesis frequency over the western north pacific, *J. Meteor. Soc. Japan*, *87*(3), 525–538, doi:10.2151/jmsj.87.525.

Zebiak, S. E., and M. A. Cane (1987), A model El Niño-Southern Oscillation, *Mon. Wea. Rev.*, *115*(10), 2262–2278.

Zhang, T., and D.-Z. Sun (2014), Enso asymmetry in cmip5 models, *J. Climate*, *27*(11), 4070–4093.

Zheng, X.-T., S.-P. Xie, L.-H. Lv, and Z.-Q. Zhou (2016), Inter-model uncertainty in ENSO amplitude change tied to Pacific ocean warming pattern, *J. Climate, in press.*

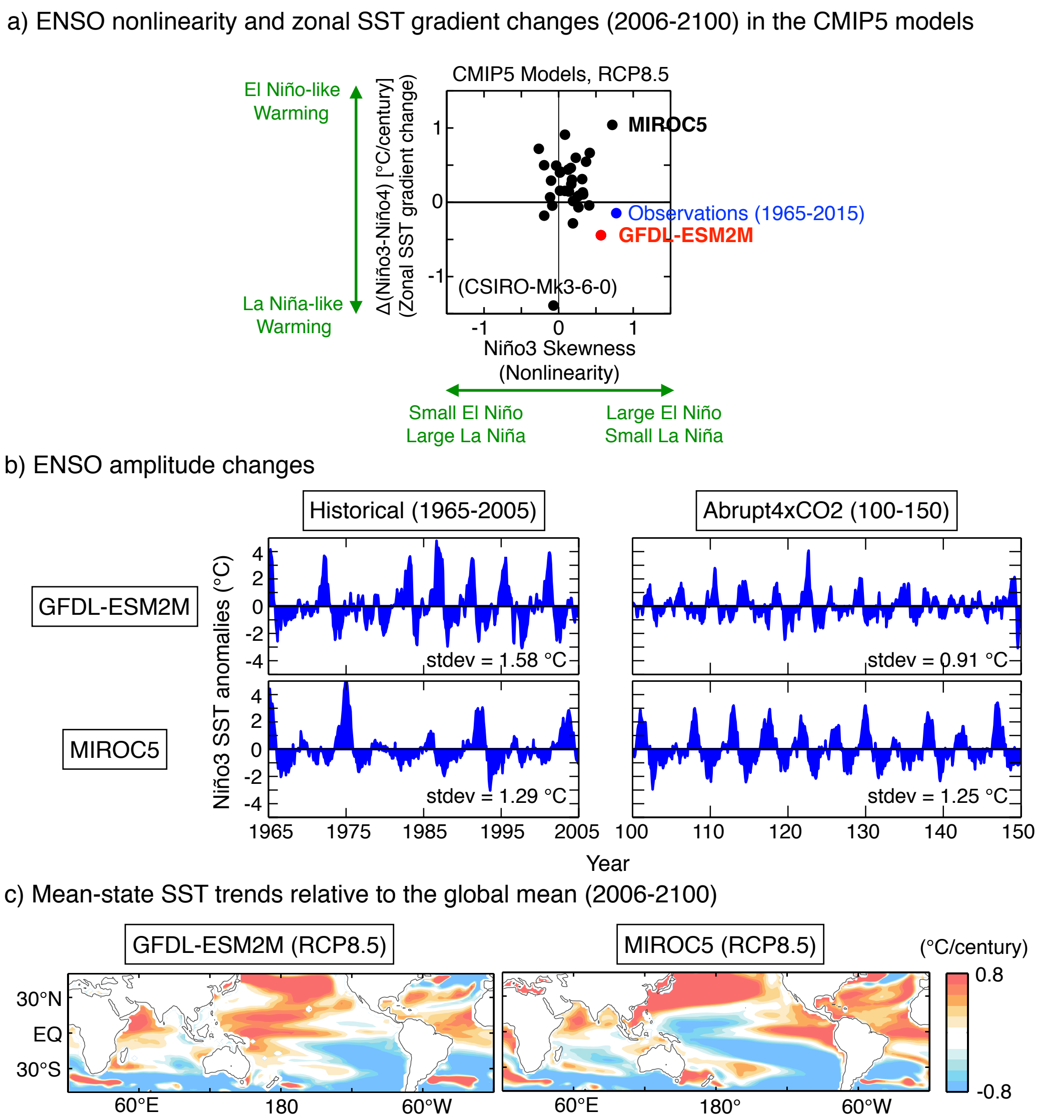

Figure 1. (a): Relationship between the Niño3 SST skewness and the zonal SST gradient change defined as the linear trend of "Niño3 minus Niño4" SST. The black and red dots represent models and the blue dot represents observations. Reproduced from *Kohyama and Hartmann* [2017]. Copyright belongs to the American Meteorological Society. (b): Monthly Niño3 SST anomalies. Standard deviations are shown at the bottom right. (c): SST warming trends calculated at each grid relative to the tropical Pacific mean trend (30°S-30°N, 90°E-60°W). Blue colors denote a warming slower than the tropical Pacific mean, not necessarily a cooling.

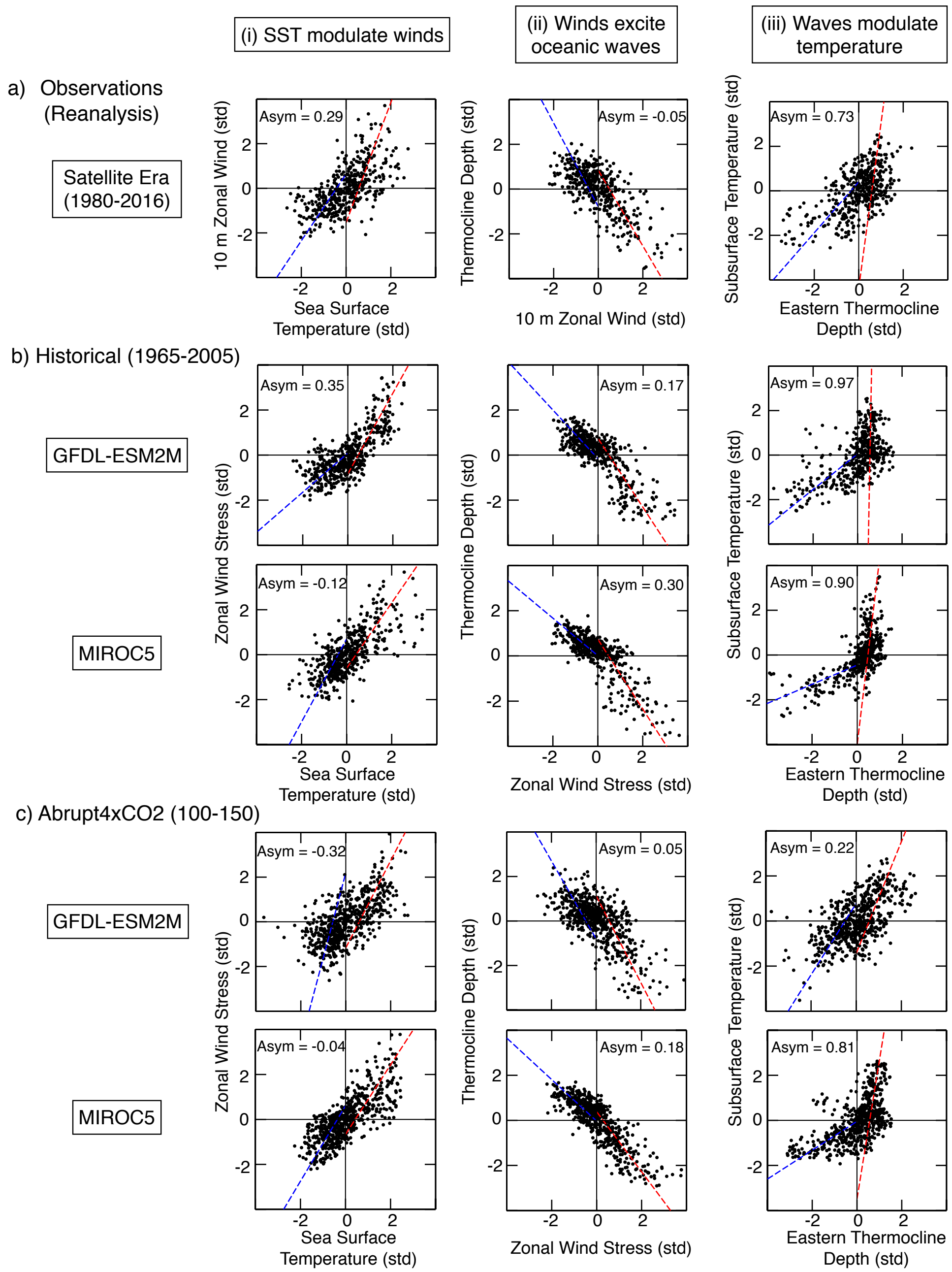

Figure 2. (a): Three potential sources of the ENSO nonlinearity presented as the observed, lagged relationships between monthly area-averaged standardized anomalies described in the axis labels. Lags are chosen to realize the maximum correlations as described in section 2.2. The values of the asymmetry index are shown at the top. The red (blue) best-fit lines are calculated using the data only with the positive (negative) values in the horizontal axis. (b): As in (a), but for models for the historical climate. (c): As in (b), but for the warmer climate.

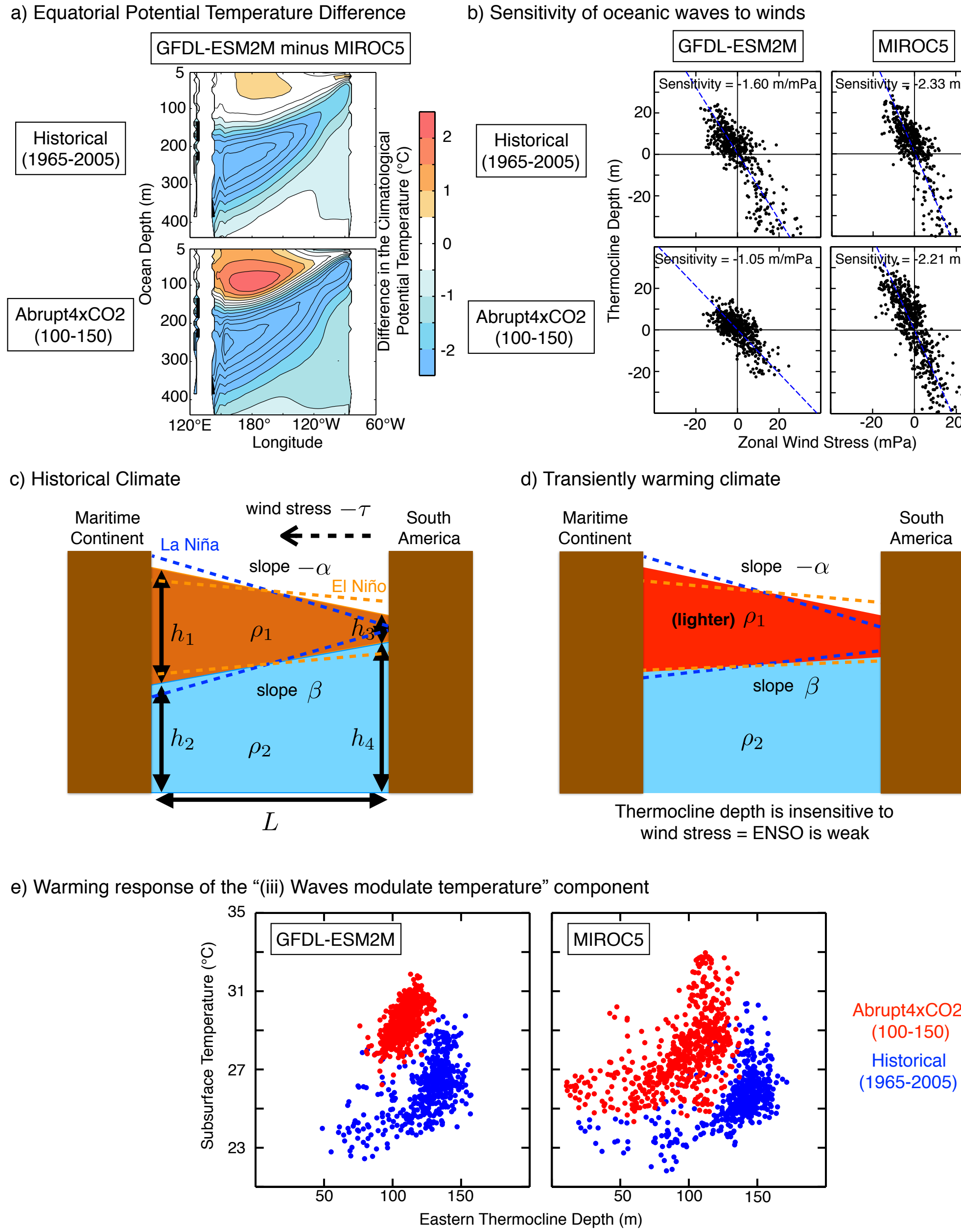

Figure 3. (a): Difference in climatological oceanic potential temperature averaged over 5°S-5°N between the two models. (b): As in the middle column of Figs. 2b and 2c, but with physical units. The best-fit lines are calculated using the entire data, and the slopes are shown at the top. (c): Schematic showing the relationship between the slope of the ocean surface and thermocline for the historical climate. (d): As in (c), but for the transiently warming climate. (e): As in the right column of Figs. 2b and 2c, but with physical units. The historical and warmer experiments are shown in the same plot.

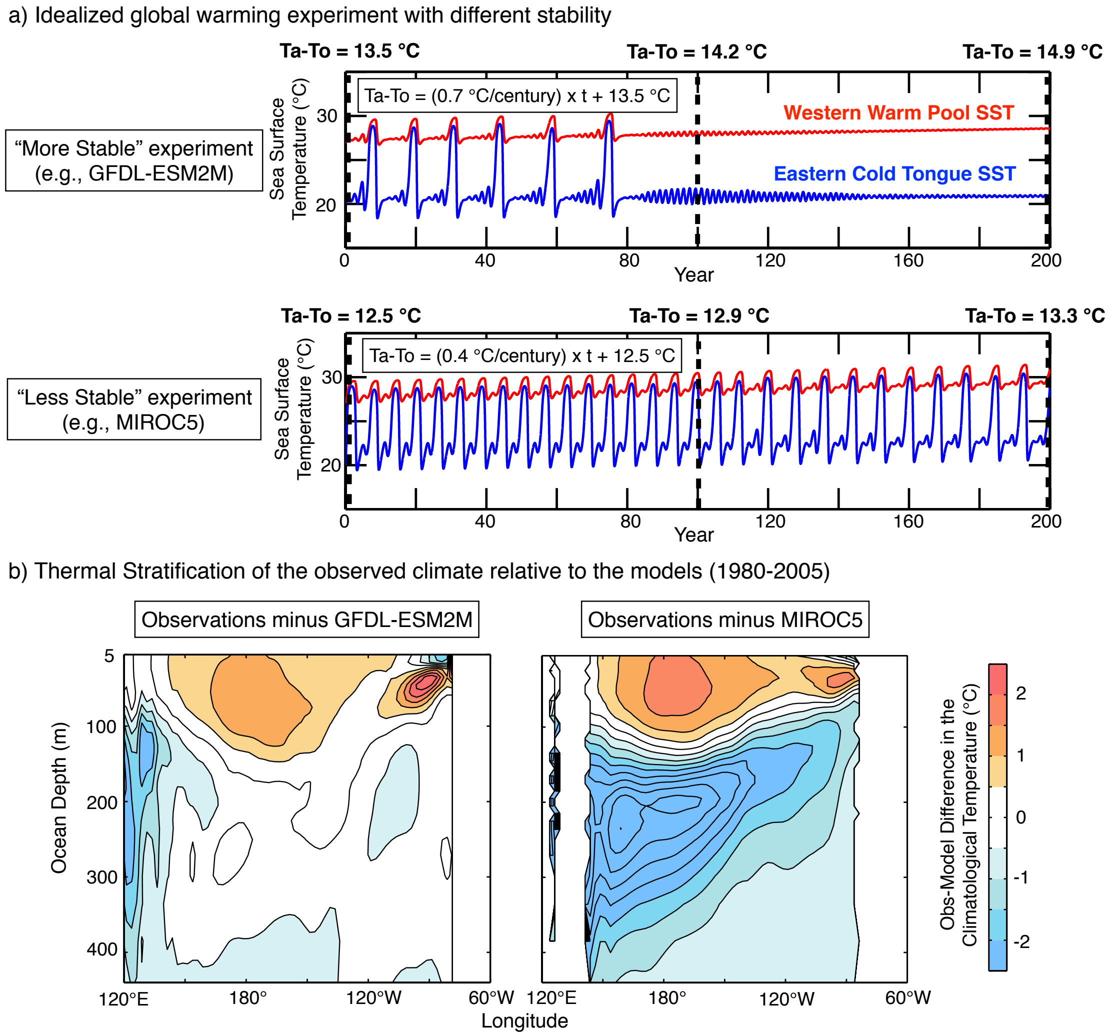

Figure 4. (a): Idealized model experiments that simulate the western (red) and eastern (blue) SST variability. The climatological reservoir temperature difference between the atmosphere near the surface and the ocean below the thermocline ($T_a - T_o$) is gradually increased with the rate shown at the top left. (b): As in Fig. 3a, but the difference between observations and models in the late historical period (1980-2005).